scientific reports

Check for updates

OPEN

Optimising 4D imaging of fast-oscillating structures using X-ray microtomography with retrospective gating

Antoine Klos[1,2], Lucie Bailly[1✉], Sabine Rolland du Roscoat[1], Laurent Orgéas[1], Nathalie Henrich Bernardoni[2], Ludovic Broche[3] & Andrew King[4]

Imaging the internal architecture of fast-vibrating structures at micrometer scale and kilohertz frequencies poses great challenges for numerous applications, including the study of biological oscillators, mechanical testing of materials, and process engineering. Over the past decade, X-ray microtomography with retrospective gating has shown very promising advances in meeting these challenges. However, breakthroughs are still expected in acquisition and reconstruction procedures to keep improving the spatiotemporal resolution, and study the mechanics of fast-vibrating multiscale structures. Thereby, this works aims to improve this imaging technique by minimising streaking and motion blur artefacts through the optimisation of experimental parameters. For that purpose, we have coupled a numerical approach relying on tomography simulation with vibrating particles with known and ideal 3D geometry (micro-spheres or fibres) with experimental campaigns. These were carried out on soft composites, imaged in synchrotron X-ray beamlines while oscillating up to 400 Hz, thanks to a custom-developed vibromechanical device. This approach yields homogeneous angular sampling of projections and gives reliable predictions of image quality degradation due to motion blur. By overcoming several technical and scientific barriers limiting the feasibility and reproducibility of such investigations, we provide guidelines to enhance gated-CT 4D imaging for the analysis of heterogeneous, high-frequency oscillating materials.

Vibratory motions are ubiquitous in biological processes as well as in mechanical engineering. From low-frequency respiratory or cardiac muscular patterns[1–3] to high-frequency sound-induced[4,5] or flow-induced[6,7] vibrations, they cover a broad spectrum of both spatial and temporal scales. Their quasi-periodicity offers the possibility to develop dedicated imaging techniques to study their evolution, which could hardly be imaged otherwise. Thus, stroboscopic methods have been designed to recover an averaged representation of the motion from multiple oscillation periods. In particular, videostroboscopy is one of these pioneering techniques, first developed in the 1950s to image human vocal folds during phonation[8–11] – these structures can vibrate between 50 Hz up to 1500 Hz, with average values of 125 Hz and 210 Hz for men and women's speech, respectively[6,12]. Videostroboscopy is now daily used in clinical voice assessment[13,14]. However, this practice only gives access to 2D views of the external surfaces of the vibrating systems (2D + time). In any case, their internal structure and its evolution remains inaccessible to measurement[15]. To address this limitation, a few previous studies have combined videostroboscopy with X-ray radiographic imaging[16–18]. Oscillating internal motions have thus become observable, albeit with a visualisation restricted to defined projection direction, and it is disturbed by the superimposed structures.

In order to access the full 3D motion, studies took advantage of the stroboscopic imaging in X-ray Computed Tomography (CT). Indeed, even the current highest acquisition speed in conventional CT—i.e., 1000 tomographies per second (tps) in synchrotron[19] with a limited field of view (528×120 px) and an extreme sample rotation

---

[1]Univ. Grenoble Alpes, CNRS, Grenoble INP, 3SR, 38000 Grenoble, France. [2]Univ. Grenoble Alpes, CNRS, Grenoble INP, GIPSA-lab, 38000 Grenoble, France. [3]ID19 beamline, ESRF - The European Synchrotron, CS 40220, 38043 Grenoble, France. [4]PSICHE beamline, Synchrotron SOLEIL, F-91190 Saint-Aubin, France. ✉email: lucie.bailly@3sr-grenoble.fr

speed (500 Hz)—is not suitable for continuous imaging of movements faster than the time needed to acquire a sufficient collection of angular projections[20–26]. Moreover, the X-ray dose and such extreme acceleration of the sample can distort the movement studied.

The first attempts at stroboscopic X-ray imaging were implemented for medical applications, to measure lung and heart function by analysing low-frequency 3D tissue motion[1,2,27–29]. Such oscillations are not regular over time, so naive stroboscopic methods were not directly applicable. Instead, two adaptive approaches were designed, based on either prospective[1,2,30–33] or retrospective gating[4,5,21,28,34–38]. Both methods require the additional acquisition of a so-called *gating signal*, which is a temporal representation of the oscillating movement. For prospective gating, the signal is monitored in real time to trigger the projection acquisition at pre-defined events[1,30] (such as the maximum amplitude of an electrocardiogram). For retrospecting gating, projections are acquired at constant rate, and sorted *a posteriori* according to the on-going motion phase at the time of their exposure, which is given by the analysis of the gating signal[28,37]. Numerous variants of gating-based X-ray tomography (or gated-CT) have been experimented since the first studies in the early 2000s. Basically, they follow the same progress as conventional X-ray tomography, proposing different scan and rotation schemes[32,39,40] (e.g., helical, cine, step-by-step, half-tomography, *etc.*), phase retrieval methods[38,41,42] (e.g., propagation-based, grating interferometry, *etc.*), and benefiting from the same advances of X-ray sources and imaging instrumentation in terms of spatiotemporal performances[33,43,44]. Besides, the image analysis methods commonly used for X-ray tomography data[45] also remain applicable to such imaging technique. Recent studies demonstrated that the conjugated use of high brilliance synchrotron facilities and judicious gating strategies allow the spatial and temporal resolutions to be improved at least by one order of magnitude each[38,40,46]. Thus, high frequency oscillations were imaged in 3D, such as the motion of blowfly steering muscles during its 150 Hz wingbeats[21,38] at a voxel size of 3.3 μm, or the sound-induced vibrations of fish inner ear[4] up to 450 Hz and a voxel size of 2.75 μm. Other works also successfully applied pure stroboscopic CT on fully controlled periodic oscillations, such as for cyclic compression-tension tests[42,47,48], or fluid mechanics experiments[49].

Although these studies gave interesting results, acquisition parameters specific to gated-CT are often determined empirically[21,38], which causes difficulty to transfer them to any multiscale oscillator. Prior methods have been suggested[50], but they were limited to low-frequency movements (i.e., below 10 Hz), and more importantly, they did not propose any guidelines to mitigate motion and streaking artefacts on reconstructed data, caused by the inherent motion and the irregular sampling of the projection space[32,36,51–53]. Hence, the current challenge in optimising gated-CT in the case of fast-oscillating structures is to understand the link between the numerous acquisition parameters involved, and the induced artefacts that can arise on the data.

To address this issue, we have developed an optimisation procedure based on the dialogue between a numerical approach and experimental campaigns carried out with oscillating composite materials in synchrotron X-ray tomographs.

On the one hand, the numerical study relies on tomographic simulations at the scale of the composite reinforcement of known and ideal 3D geometries, such as sphere or fibre. The objective is to reproduce and quantify motion artefacts due to the imaging process. Besides, a method to ensure a quasi-equi-angular sampling of the projection space is also proposed.

On the other hand, gated-CT of soft composite samples subjected to rigid body oscillation were conducted thanks to a custom-developed vibromechanical test rig with a continuous rotation and retrospective gating strategy. Finally, by comparing real and virtual 4D data using image quality indices, the relevance of the methodology was evaluated at various time and spatial scales.

Guidelines towards the optimisation of imaging parameters
Problem statement
Let us consider a heterogeneous medium (e.g., a composite material made of spherical or fibrous inclusions embedded into a matrix) subjected to a sinusoidal rigid body translation, and the 3D motions and evolving microstructure of which are to be characterised. More precisely, we seek to obtain a discrete sequence of the oscillation cycle into a given number N of phases, as illustrated in Fig. 1a,b. For this purpose, retrospectively gated X-ray microtomography can be combined with a continuous-rotation scanning strategy. As previously described by Ford et al.[37], the global experimental procedure of such technique relies on four major steps (Fig. 1b,c): (1) the continuous recording of a gating signal representative of the studied periodic motion; (2) the synchronised acquisition of 2D projections; (3) the gating-based sorting of the projections into N phases; (4) 3D image reconstruction of all phases of the oscillation cycle. Process feasibility and 4D (3D + time) image quality will depend on a series of parameters related to X-ray scanning settings and sample geometry and kinematics. These aspects are detailed below and reported in Fig. 1a–c.

- *X-ray scanning parameters:* voxel edge length L_{vx}, also known as "pixel size"; synchrotron-beam mean energy for adequate contrast on 3D reconstructed datasets, E; projection sampling rate f_s; total number of projections to be recorded to reconstruct N volumes, n^{tot}.
- *Geometrical parameters:* characteristic sample size L, defined as its maximum thickness along the X-ray beam path; average size of the heterogeneities within the sample, d_0.
- *Kinematical parameters:* mean oscillation frequency f_0; peak-to-peak oscillation amplitude A.

These parameters are independent, but their values indirectly drive the measurement spatial and temporal resolutions. Spatial resolution refers to the minimum distance required to separate two object features[54,55]. In conventional tomography, it is partly related to L_{vx}. Temporal resolution refers to the timestep between consecutive tomographic reconstructed 3D images[56]. In the following, it also corresponds to the duration of one phase
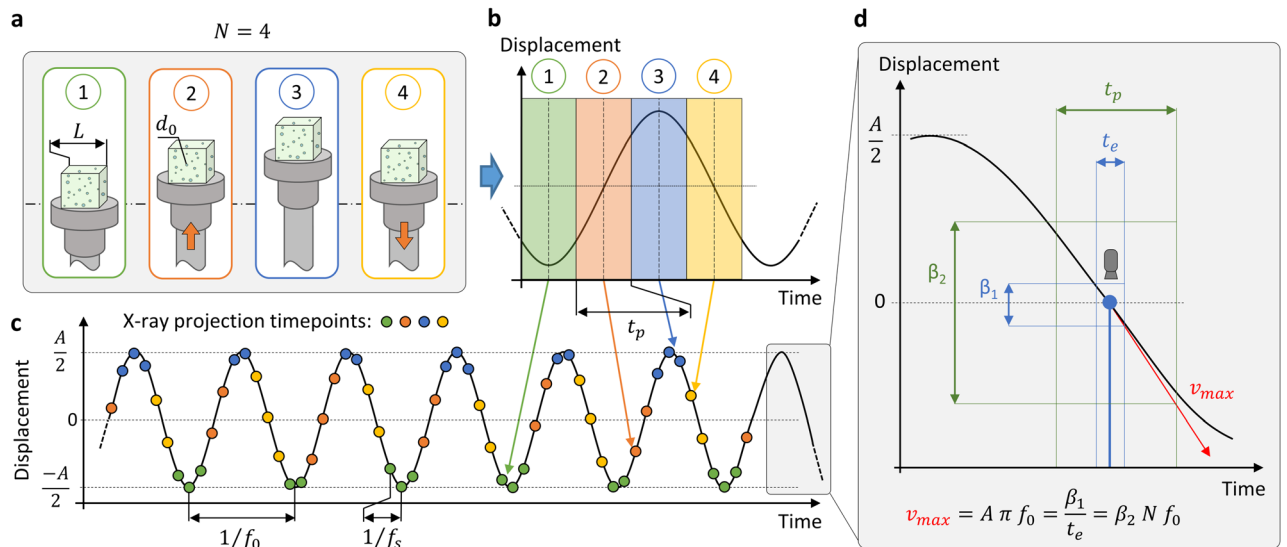
Figure 1. (**a**) Illustration of $N = 4$ phases of a cubic sample subjected to a rigid body oscillation. (**b**) Representation of a typical oscillation period splitted into $N = 4$ temporal phases. (**c**) Illustration of the phase-based projection sorting procedure for retrospectively gated-CT. (**d**) Definition of β_1, β_2 and v_{max} on a detailed view inside an oscillation period. The times t_e and t_p are arbitrary. The red arrow represents the maximum slope during sinusoidal motion, and the blue point a projection acquisition shot-instant.

$t_p = (N f_0)^{-1}$ (Fig. 1b). Therefrom, what are the optimal values to assign to all the above parameters to satisfy a targeted temporal resolution?

In order to obtain the image quality needed to quantify microstructural features or local kinematic measurements[57,58], previous works have already provided recommendations for the choice of certain parameters such as pixel size and number of projections[56,59,60]. Although these insights were applied in the case of (quasi-)static experiments, we make the assumption that they are good candidates for gated-CT as well. Therefore, as the image quality depends partly on the number of projections used to reconstruct the 3D dataset based on filtered backprojection approaches, the number of equally spaced projections over a full rotation is chosen based on the commonly accepted rule[59]: $n = \pi L/(2L_{vx})$. Naturally, it then comes $n^{tot} = Nn$. Furthermore, in order to be able to carry out a correct quantification of microstructural parameters, it was demonstrated that heterogeneities have to be sufficiently resolved, i.e., with minimal ratio d_0/L_{vx} around 5[56,60].

In the following, to reduce the number of variables to be optimised, we suggest to fix geometrical parameters, oscillation frequency f_0, beam energy E, voxel size L_{vx} and temporal resolution t_p (N, n and n^{tot} being thus directly deduced from the above equations). Thereby, we focus on quantifying the effect of oscillation amplitude A and projection sampling rate f_s on the feasibility of the experiment, as well as on the quality of the obtained 4D data. The objective is to propose the user an optimal choice of these parameters, further noted A^* and f_s^*, as detailed in the next sections.

Vibratory amplitude and motion artefacts

Motion blur descriptors
Depending on the kinematical and X-ray scanning parameters, several motion artefacts may alter the reconstructed 3D dataset, yielding to blurred images with undesired information loss[51]. Artifacts become more pronounced as sample speed increases. More specifically, knowing the maximal displacement velocity achieved by the sample during its periodic movement v_{max}, two different types of motion blur can be defined, as illustrated in Fig. 1d:

(i) a motion blur directly induced during 2D projections recording, resulting from the relative displacement between the sample and the image sensor during the beam exposure time per projection, t_e. In the following, this motion blur is noted β_1. Its maximal magnitude is fairly estimated by the displacement of an object that would move linearly at speed v_{max} during t_e: $\beta_1 = A \pi f_0 t_e$.

(ii) a motion blur induced during the reconstruction of the 3D data, resulting from the retrospective gating technique and the temporal resolution t_p used to reconstruct the cycle. Namely, the gathered projections are not taken at the exact same location of an oscillation period (Fig. 1b,c). In the following, this motion blur is noted β_2. It is estimated by the displacement of an object that would move linearly at speed v_{max} during t_p: $\beta_2 = A \pi /N$.

*Limitation of the motion blur*
By definition, both blur descriptors β_1 and β_2 are linked with A, f_0, N and t_e (Fig. 1d)— f_0 and N being fixed at this stage. The exposure time t_e is adjusted prior a gated-CT by performing a series of conventional CT on the sample

3

at rest, under similar scan conditions (i.e., with n projections, a beam energy E, a pixel size L_{vx}). The shortest value of t_e resulting in an image quality that allows an accurate quantification is then retained. Once t_e is fixed, the motion blur descriptors β_1 and β_2 only depend on the peak-to-peak amplitude of the prescribed sinusoidal motion, A. In the following, we will estimate the critical values β_1^* and β_2^* of these descriptors that must not be exceeded to enable a given quantitative analysis of the images. This will be achieved with the help of a numerical work, by simulating the blurring artefacts at the scale of particles with known and ideal 3D geometry (sphere or fibre) for different couples (β_1, β_2), and by quantifying the final image quality compared to a static reference configuration. Finally, this approach will lead to the proposal of an acceptable oscillation amplitude A^* for the user.

Optimisation of the angular sampling of projections

In order to prevent reconstruction artefacts such as streaks and missing boundaries[32,36,52,61–63], two main aspects should be considered: (i) the total number of projections, n^{tot} should be equally distributed between the N phases; (ii) within each phase, the angular sampling of the projections should be regular. Both conditions are directly influenced by the projection sampling rate f_s. It is therefore necessary to understand how to select this parameter while restraining the above artefacts. In the first instance, one could choose f_s as high as possible. However, depending on f_0, projections for all the phases may not be acquired (see case II, Fig. 2). Therefore, the proposed optimisation relies on the requirement to periodically acquire at least one projection in each of the N phases. With this aim, we first introduce $i \geq N\,(t_e + t_l)\,f_0$, where $i \in \mathbb{N}_{\neq 0}$, is the number of oscillation periods of the sample needed to acquire at least one projection in each of the N phases and where t_l is the minimum latency time between two consecutive exposures (typically equal to the detector readout time). In practice, we choose i as the smallest integer possible such as $i = \lceil N(t_e + t_l)f_0 \rceil$ to minimise the acquisition duration, except if this leads to a projection sampling rate that requires an unattainable speed of the rotation stage ω – which is directly derived
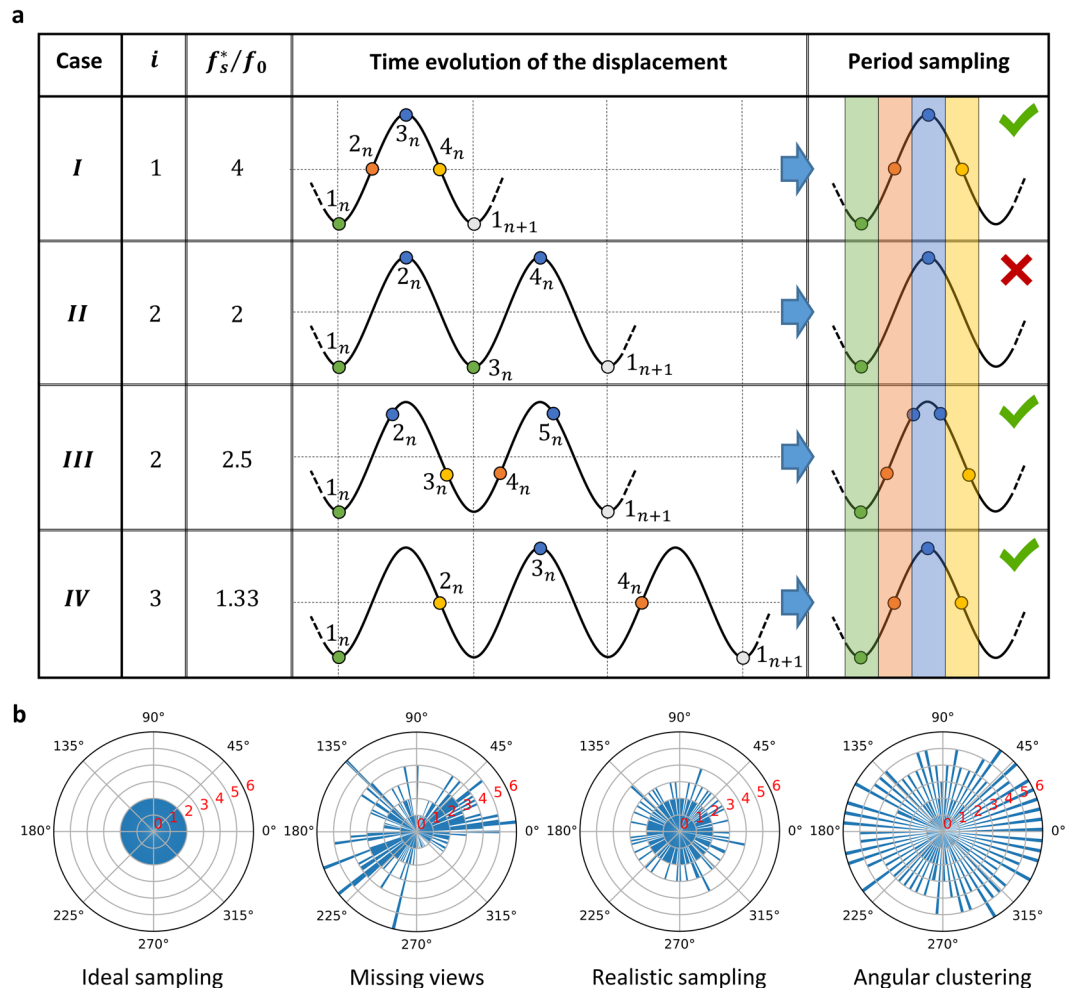
Figure 2. (**a**) Scheme of the different cases for the optimisation of the projection sampling rate, f_s. $N = 4$. (**b**) Polar histograms of typical angular distribution of the projections of a phase after the sorting process, for illustration purposes. The angle represents the angular position of the projections and the radial axis the number of projections per bin (n = 360 projections, bin width = 2°). The ideal sampling is generally obtained in conventional CT. Angular clustering and missing views distribution produce strong image artefacts.

from f_s and n^{tot}. As possible examples, Fig. 2a displays various acquisition cases, yielding to distinct values of i in the case where $N = 4$. Then, to meet the above requirements, the optimal f_s^* must fulfil the following condition:

$$\exists \{k \in \mathbb{N} \mid k \geq N\}, \quad \text{such as} \quad f_s^* = \frac{k}{i} f_0 \quad \text{with} \quad \begin{cases} k = N & \text{if} \quad i = 1 \\ k \bmod i \neq 0 & \text{if} \quad i > 1 \end{cases} \tag{1}$$

where k includes an anti-aliasing correction as a function of the selected value of i.

Cases I and II shown in Fig. 2a describe the examples where $i = 1$ and $i = 2$, respectively. Therefore, case I shows an appropriate sampling of all the N phases within one oscillation period, whereas case II depicts a wrong sampling which will result in unusable data, characterised by irregular angular distribution of projections possibly combined with angular projection clustering, as illustrated in Fig. 2b. Cases III and IV both show alternatives to remedy this problem, and together with case I, they should produce a relatively regular sampling of projections ("realistic sampling", Fig. 2b), close to the one obtained in conventional tomography ("ideal sampling").

The best choice between cases I, III and IV will then depend on the experimental constraints of each study. For example, ideal case I requires compatible detector performances, whereas case III implies a shorter acquisition duration so a lower radiation dose compared to case IV, which, in turn, could give better projection distribution between the phases. Thus, in the following, when case I was not applicable, we chose case III in order to prevent the effect of the dose on specimen, although for many experiments the dose involved is not prohibitive.

Finally, note that in practice, once f_s^* is found, the latency time between two consecutive exposures t_l^*, is such that $t_l^* = (1/f_s^*) - t_e$. This latency time can then be taken into account when triggering the detector.

Methods

The general concept and optimisation strategy of imaging parameters presented in the previous section were assessed through a dialogue between numerical simulation and experimental data. On the one hand, the numerical simulation focused on blurring artefacts at the scale of ideal spherical or fibrous inclusions used in composites. On the other hand, a series of gated-CT experiments were carried out on soft silicone composites filled with spherical or fibrous particles, using *a priori* optimal scanning parameters, as detailed below.

Tomography simulation with motion artefacts

The tomography simulation was coded in *Python*, following a procedure illustrated in Fig. 3 for the case of spherical reinforcements. For this purpose, two 3D ideal phantoms mimicking the shape (sphere or fibre) and average size of real samples' heterogeneities were firstly designed. More specifically:

(i) a sphere with a dimensionless diameter $d_0^* = d_0/L_{vx}$ was generated thanks to the module *Kalisphera* from the *spam* software[57,64]. In particular, a sphere with $d_0^* = 4$ was designed centered in a field of view (FOV) of 11×11×31 vx (black background).

(ii) a fibre-shaped phantom with a dimensionless diameter of d_0^* and a dimensionless length of $l_0^* = 25d_0^*$ was designed and oriented perpendicularly to the rotation axis (z axis). In particular, a fibre with $d_0^* = 2$ and $l_0^* = 50$ was designed centered in a FOV of 61×61×31 vx (see Supplementary Fig. S1).

Note that for both cases, a specific caution was paid on the particle-matrix interface, to simulate the partial-volume effect[64] which arises in volumetric images when more than one material occurs in a voxel, and which is more pronounced when the heterogeneity size d_0 is close to L_{vx}, i.e., when $d_0^* \approx 1$.

Then, for each case, a blurred 3D phantom with given motion artefacts (β_1, β_2) was designed, as illustrated in Fig. 3 for the case of a sphere. To do so:
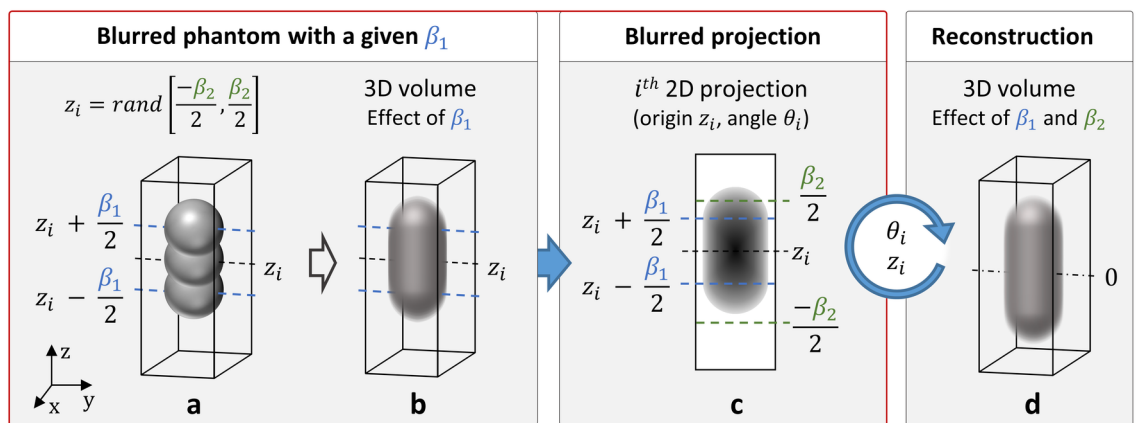
Figure 3. Procedure used for tomography simulation on a spherical phantom for a given couple of motion blur descriptors. The effect of β_1 is visible when generating the projections whereas the one of β_2 is only observable after the reconstruction.

- At first, an initially ideal and smooth 3D particle was designed at a given position $\mathbf{X}_i(0,0,z_i)$, whose height z_i was randomly chosen within a β_2-interval. From this ideal particle, $10 \times \beta_1$ sub-phantoms were replicated and evenly distributed along the z-axis, over a β_1-interval centered on z_i (see Fig. 3a). Therefrom, a first blurred 3D phantom was generated by averaging all the sub-phantoms to simulate a given motion blur β_1, as illustrated in Fig. 3b.
- Then, the *Astra-Toolbox*[65–67] package was used to generate a single projection of this preliminary blurred phantom, considering a parallel beam (see Fig. 3c). This projection was chosen at an angular position θ_i, $i \in [1..360°]$. Note that, in order to focus only on the effect of the motion blur on image quality and to avoid other artefacts, we chose to oversample the projection domain (360 projections) and to not restrain artificial numeric noise.
- Finally, steps (a) to (c) were repeated for all z_i in the β_2-interval and θ_i, yielding to a series of 360 projections in total. Thus, a 3D volume simulating both target blur descriptors β_1 and β_2 could be reconstructed, using a filtered backprojection algorithm with the same package (see Fig. 3d).

The motion blurs β_1 and β_2 were both varied between 0 and 10 px with a 0.5 px step, resulting in a total of 441 simulated tomographies for each phantom.

Experimental developments

Sample preparation

We fabricated composite samples made of a soft deformable silicone matrix (a two component addition-cure rubber compound Ecoflex[TM] 00-30, Smooth-On; relative density 1.07) reinforced with either solid glass beads (Silibeads[®] SOLID, Sigmund Lindner, density ≈ 2.5 with a mean diameter $d_0 \approx 40\ \mu$m; Fig. 4d), or chopped fibreglass (Conrad[®], ref. 2101101, with mean dimensions $d_0^* = 20\ \mu$m and $l_0^* \approx 10\ d_0^*$). In any case, the volume fraction of particles was prescribed at $\approx 5\%$. Samples were prepared as follows. Firstly, the two compounds of the liquid silicone were mixed with a 1A:1B mixing ratio by weight. Then, particles were added and mixed at the defined volume fraction. The resulting mixture was poured in a Petri dish to obtain a 2 mm-thick bulk, and immediately degassed in a vacuum environment for 5 min at 8×10^3 Pa to eliminate air bubbles. Afterwards, it was left for curing at room temperature (T $\approx 21°$C) during 24 h, covered to prevent external pollution, and laid
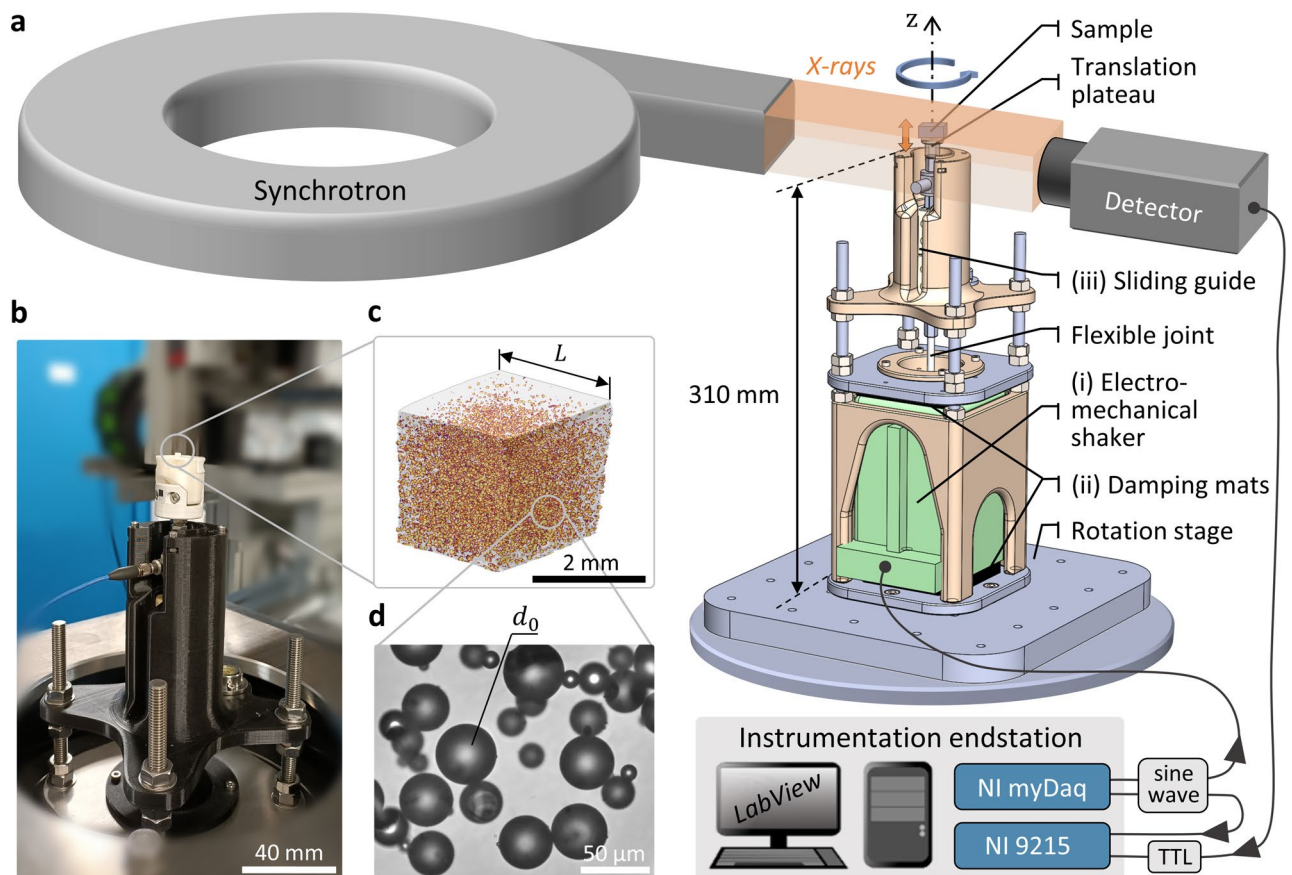
Figure 4. (**a**) Schematic view of the vibratory setup and its simplified wiring diagram during *in situ* testing on the PSICHE beamline. (**b**) Picture of the setup on the motorised rotation stage. To deal with space requirement the setup was inserted inside the hollow stage. (**c**) 3D rendering of the imaged sample. (**d**) Optical microscopy image of a representative distribution of the glass beads filling the sample.

	Geometry		Kinematics				X-ray settings			
	L	d_0	f_0	A^*	β_1^*	β_2^*	L_{vx}	f_s^*	t_e	n^{tot}
	(µm)	(µm)	(Hz)	(px)	(px)	(px)	(µm)	(Hz)	(s)	
C1	2000	≈ 40	100	≈ 11	≈ 2.5	≈ 1	9.58	1033	0.8×10^{-3}	10,000
C2				≈ 24	≈ 6	≈ 2.5				
C3				≈ 34	≈ 8.5	≈ 3.5				

Table 1. Experimental parameters used for the three case studies **Ci**, $i \in [1..3]$. All values marked with "*" were derived from the optimisation procedure. Note that the values reported here for β_1^*, β_2^* and A^* were chosen *a priori* from these guidelines, albeit re-evaluated *a posteriori* on the recorded images, and rounded to the nearest half-pixel. In all cases **Ci**, $\beta_1^*/\beta_2^* \approx 2.5$.

on a flat surface to obtain a uniform thickness. Right before the X-ray experiment, the specimens were cut from the bulk using a scalpel to obtain cuboid samples of edge size $L = 2$ mm, as shown in Fig. 4c.

Vibratory setup
A custom vibro-mechanical setup was designed to subject samples to sinusoidal rigid body translation by controlling oscillation frequency f_0 and amplitude A (Fig. 4). The excitation was performed by a small electromechanical shaker (Fig. 4a-i) with embedded amplifier (Smartshaker™ K2007E01, The Modal Shop), able to oscillate in a wide range of frequency (1–1500 Hz). The apparatus was clamped in the test bench with two layers of rubber damping mats in between (Fig. 4a-ii) to prevent the spreading of vibrations in the whole setup. At the output of the shaker, two linear plain bearings (drylin® Q, Igus) coupled with a square profile were added to ensure a translation of the exciter tip along z (Fig. 4a-iii). For each oscillation frequency of interest (f_0 varied from 1 to 400 Hz), the amplitude response of the setup was calibrated as a function of the input sinusoidal voltage (variations within ± 1 V) with a laser doppler vibrometer (VibroFlex® Xtra VFX-I-120, Polytec). The oscillatory amplitude could be tuned between a few µm up to 13 mm at lowest frequencies. The control of the applied sine wave was made through a *LabView* program, and a *National Instruments* device (NI myDAQ). An acquisition device (NI 9215) was used to acquire the control signal at 100 kHz and the Transistor-Transistor Logic (TTL) signal that came from the microtomograph's detector which provides the time of projections for synchronisation purpose (see Fig. 4a).

Mechanical tests
As a first step, in order to assess the degradation of image quality due to motion artefacts, tests were carried out on a single composite reinforced with spherical glass beads, vibrating at a fixed frequency $f_0 = 100$ Hz, but with different amplitudes A^* as derived from the theoretical guidelines detailed above. More specifically, three experimental cases (**C1**, **C2**, **C3**) were considered sequentially, while progressively increasing the critical pairs (β_1^*, β_2^*) from about (2.5 px, 1 px) up to (8.5 px, 3.5 px), and thus, the prescribed amplitude A^* from 11 to 34 px (i.e. 105 to 326 µm for a pixel size $L_{vx} \approx 9.58$ µm - see details below on the imaging setup). The experimental parameters for each case are resumed in Table 1.

In a second step, in order to assess the relevance of the measurement strategy more widely, other vibration tests were extended to another particle shape (fibre) and to a higher oscillation frequency $f_0 = 400$ Hz.

Acquisition procedure and synchrotron X-ray instrumentation
Samples were imaged at the PSICHE beamline of the SOLEIL synchrotron[68] (Saint-Aubin, France). The optical setups were chosen to image each composite sample both at rest (scans named as *static reference* in the following) and while vibrating with a target number of $N = 30$ phases to be captured.

Beamline configuration—High-energy photons (15–100 keV) were produced from a in-vacuum wiggler (fixed gap 4.5 mm) and filtered using an X-ray mirror (Ir surface, 1.9 mrad angle)[69], combined with a set of filters to adjust the energy spectrum for *pink* beam illumination. The imaging configuration leads to a pixel size of $L_{vx} = 9.58$ µm, with a FOV = 400×400×320 vx. The exposure time per projection t_e, was set to 0.2 or 0.8 ms depending on the case under study. The mean photon energy was set to $E = 30.3$ keV (wavelength = 0.409 Å) with a flux of 2.30×10^{12} photon mm^{-2}s^{-1} (obtained with 3.5 mm Al and 0.735 mm Sn filters) for $t_e \approx 0.2$ ms, and a flux of 0.96×10^{12} photon mm^{-2}s^{-1} (with 3.5 mm Al and 0.608 mm Sn filters) for $t_e \approx 0.8$ ms. To convert the transmitted X-rays into visible light, a 250 µm-thick Ce-doped LuAG scintillator was placed behind the sample at a propagation distance of 700 mm which resulted in an optimal combination of absorption and phase contrast. Radiographic projections were acquired with a pco.Dimax CMOS HS4 (pixel size = 11×11 µm²) detector mounted on a tandem optic composed of two Hasselblad HC 2.2 / 100 mm lenses.

Gated-CT acquisition procedure—The acquisition procedure consisted of a continuous 360°-rotation of the sample stage along the z-axis (Fig. 4a), while acquiring $n^{tot} = 10,000$ projections. In practice, the rotation velocity ω was about 37°s^{-1}, which corresponds to 10 s for the acquisition of a complete gated-CT with $N = 30$ (i.e., ≈ 330 ms to scan a single 3D volume). The optimised projection sampling rate f_s^* was calculated at 1,033 Hz (Table 1), based on Eq. 1 and selecting case III in Fig. 2. Besides, although a 180°-rotation is *a priori* sufficient to capture a stable oscillation, a multi-rotation approach was chosen here as scanning strategy (i.e., two successive half-turns), to reduce the risk of too many missing views in the event of periodic oscillation being interrupted during the experiment, which would compromise the feasibility of 3D image reconstruction[21]. As shown by

Walker et al.[38], this multi-rotation strategy is especially relevant to capture transient phenomena. In our study, unexpected transient events can result from instrumentation failure, material damage or thermal expansion due to the X-ray dose. Finally, this full-turn acquisition was a trade-off between the aforementioned aspect, the technical limit of the rotation stage, the avoidance of inertial effects due to the rotation velocity[19,21], and the limitation of rotational motion during X-ray exposures.

Data post-processing
Retrospective gating and projections sorting
After scanning, all projections were sorted according to the current oscillation phase at the time of their exposure, so as to redistribute them into $N = 30$ phases of one periodic cycle (Fig. 1b). This step relies on the measurement of the duration of successive cycles of a gating signal representative of the motion temporal evolution. In practice, we used the control sinusoidal voltage of the electromechanical shaker as gating signal, and cycles were arbitrarily defined between consecutive valleys of the gating sine wave. Of course, a constant phase shift may exist between the gating signal and the actual motion, albeit without any consequences for the following steps. The phase-based sorting algorithm we employed is illustrated in Fig. 1c.

Tomographic reconstruction
The reconstruction of each 3D volume relative to one temporal phase was performed with the *PyHST* software[70] using a filtered backprojection algorithm coupled with Paganin's method for phase retrieval[41] with a kernel length of 7 px. The center of rotation (COR) of the N datasets was defined manually, using the one given by an automatic COR detection algorithm performed on the corresponding *static reference* 3D image.

Quality of the 3D images
Rigid volume registration—In order to perform a reliable pairwise comparison of the quality of the images obtained by scanning the same sample at rest and in vibration, a one-to-one correspondence was established between the coordinates of the N images of a reconstructed gated-CT and those of its corresponding *static reference*. The registration of the images to be compared was achieved using the *spam* software[57], which includes a global volume registration function. The registration algorithm minimises the error between the reference volume and the one deformed by Φ, a linear deformation function. The function Φ is an extension of the transformation gradient tensor, taking into account also the translation vector (t_x, t_y, t_z), which together with the rotation describes the rigid-body motion of the sample. The registration for the first phase was unsupervised, whereas the computed function Φ was given recursively as a guess for the following phases. The convergence of the registration algorithm was validated according to the criterion[57] $|\delta\Phi| \leq 10^{-3}$. The same image processing was also used to measure the 3D displacement (i.e., translations and rotations) of the sample over the 30 phases of the oscillation. In this case, the first phase was consistently considered to be at the initial position: $(t_x, t_y, t_z) = (0, 0, 0)$.

Quality indices of the CT-scans – Two metrics were investigated to assess the image quality, i.e., one based on greyscale images, and the other on thresholded images. They were chosen as representative of typical quantitative image analyses carried out on CT data[45].

- **Pearson Correlation Coefficient (PCC)**: the PCC[71] is a global measurement of the linear correlation between two greyscale images. It is defined as the covariance of the two images X and Y, divided by the product of their standard deviations (σ_X, σ_Y): $\text{PCC} = \sigma_{XY}/(\sigma_X \sigma_Y)$. It is based on the same concept as the error of digital volume correlation (DVC), but computed on the whole images. Besides, this index has the benefit of being insensitive to uniform variations in brightness or contrast that could be caused by the low variability of the number of projection n in each phase. PCC values range from -1 to 1. An absolute value of 1 means that the grey level intensities of the two 3D images are perfectly linearly related, and the sign is determined by the regression slope. On the contrary, a value of 0 means that there is no linear dependency between the images. For the specific case of simulated tomographic data, the masked ROI was defined as a centered 6 px diameter cylinder oriented along the translation axis for the 4 px diameter sphere, and a centered $53 \times 5 \times 31$ box for the fibre.
- **Segmentation Error on the Volume of Particles (SEVP)**: we define the SEVP based on the thresholded images, as the error made on the estimation of the particles volume between blurred image, V_{blur}, and its associated *static reference*, V_{ref}, so that $\text{SEVP} = |V_{blur} - V_{ref}|/V_{ref}$. Both volumes were calculated using an *Otsu* threshold[72]. This metric is sensitive to d_0/L_{vx}, as small d_0 will lead to higher SEVP[73].

Results and discussion
Guidelines provided by the simulation
Identification of critical values for motion blur descriptors
The simulated 3D images of a single ideal sphere ($d_0^* = 4$) when subjected to a series of motion blurs (β_1, β_2) are illustrated in Fig. 5a. The reconstructed slices obviously show a loss of image quality when increasing the motion blur descriptors, compared to the case predicted under static conditions, i.e., with $\beta_1 = \beta_2 = 0$. To better quantify this, Fig. 5b shows the evolution of PCC and SEVP with (β_1, β_2). Several trends are highlighted:

- Whatever the index, for $\beta_i \leq 3$ px, the two maps reported in Fig. 5b exhibit a near-plateau area where the increase of (β_1, β_2) seems to have a limited effect on the quality degradation (see the lightest yellow area in the PCC map, and the darkest blue area in the SEVP one). For larger values of β_i, the PCC (resp. SEVP) sharply decreases (resp. increases). The decrease in PCC is related to a loss of global spatial correlation due to the
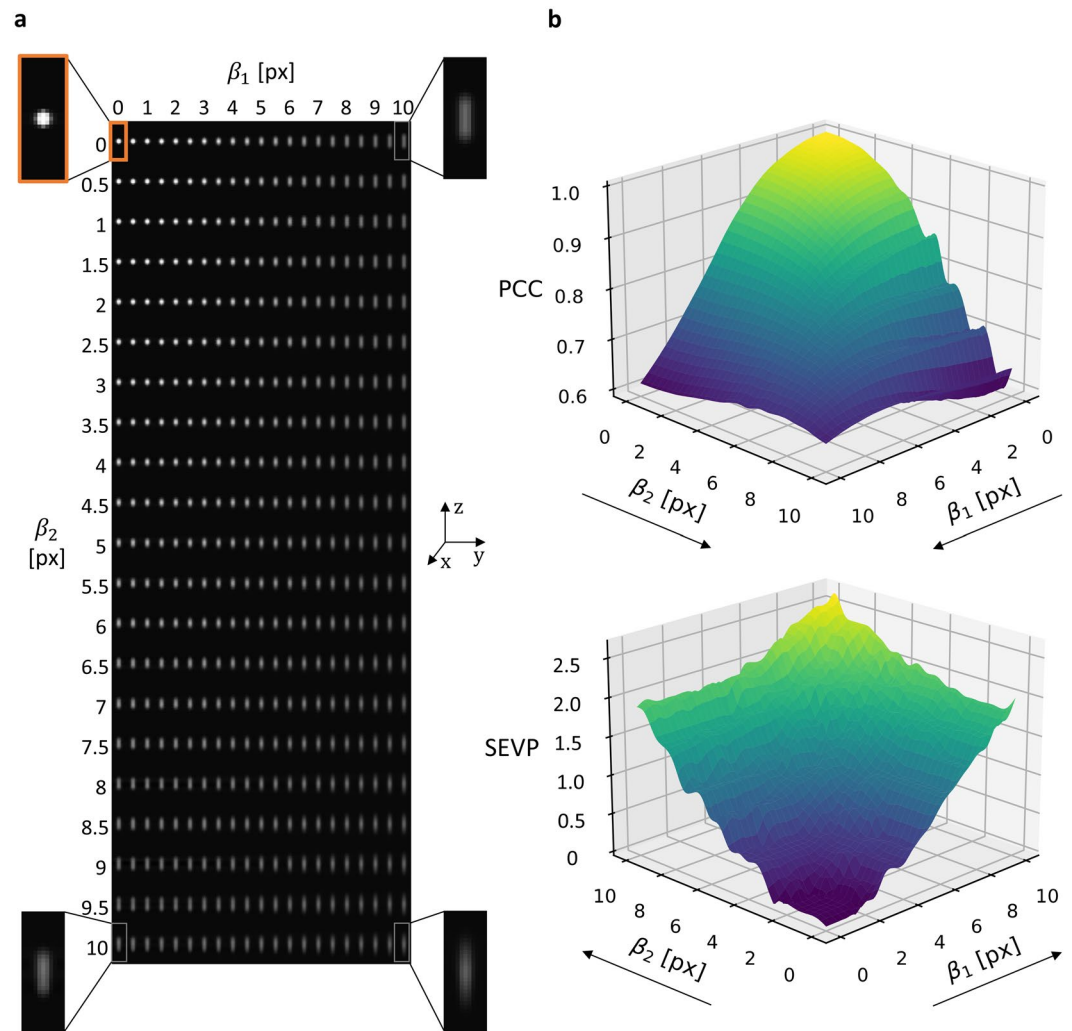
Figure 5. (**a**) Vertical slices of 3D images of a sphere ($d_0^* = 4$) obtained by tomography simulation, and artificially blurred to mimic various levels of motion artefacts β_1 and β_2. The orange box denotes the static reconstructed sphere ($\beta_1 = \beta_2 = 0$). Detailed view of the slices are given extreme couples ($\beta_1 = \beta_2 = 0$), ($\beta_1 = 10$ px,$\beta_2 = 0$), ($\beta_1 = 0$, $\beta_2 = 10$ px), ($\beta_1 = \beta_2 = 10$ px). (**b**) *(top)* 3D surface plot of the PCC computed between each blurred simulation and the static one. *(bottom)* Idem for the SEVP with switched axis for better illustration.

expansion of the blur-affected background regions, while the growth of SEVP is the result of a systematic overestimation of the particle volume as the motion artefacts change it from an ideal sphere to an oblong ellipse. Note that by definition, β_2 induces a random aspect to the spread of projections over a motion interval (see Figs. 1d, 3). This, combined with the 0.5 px sampling step of the (β_1, β_2) plane, could explain the observed fluctuations of the PCC and SEVP indices around their global trends.

- Besides, comparing the impact of one motion blur parameter *versus* the other on image degradation (i.e., β_1 *vs.* β_2), proves that there is no straightforward clue that one blur descriptor should be restricted more than the other.

- In addition, the errors induced after segmentation (SEVP) are much higher than those reported by accounting for the whole information of the greyscale native image (PCC). Typically, for the most blurred reconstruction obtained with (β_1, β_2) = (10 px, 10 px), a decay of 40% is predicted for the PCC, whereas an error of about 250% is reached for the SEVP. Such errors are exacerbated by the small value chosen for d_0 and the choice of the threshold method such as *Otsu's* one[72].

Similar results were obtained by simulating 3D images of a vibrating fibre-like phantom ($d_0^* = 2, l_0^* = 50$), albeit with even greater error levels ($\approx 80\%$ for the PCC, and 600% for the SEVP for (β_1, β_2) = (10 px, 10 px); Supplementary Fig. S1), as expected for particles of smallest diameter[73].

From this particle-scaled numerical database, critical values of motion blur descriptors not to be exceeded for an experimental design, denoted (β_1^*, β_2^*), can then be defined by thresholding the above image quality metrics (PCC and/or SEVP). More specifically, by setting these β_1^* and β_2^* values when preparing an experimental protocol, a certain level of quality indices should be expected for the acquired 4D dataset – and this, for all phases of the
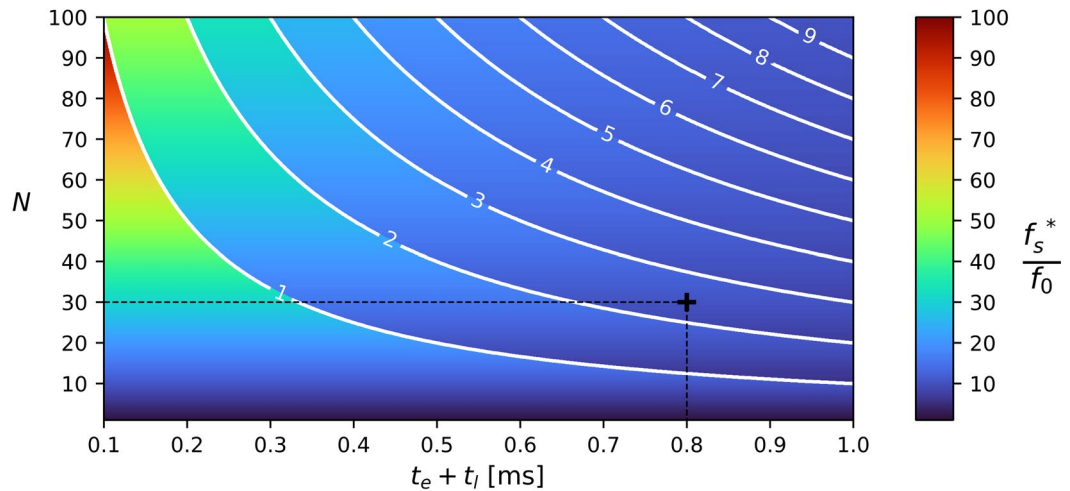
Figure 6. Optimised projection sampling rate f_s^* according to the number of phases N and to the minimum time between consecutive exposures t_l (typically close to t_e). Represented values correspond to case I if applicable or to case III otherwise (Fig. 2a), for $f_0 = 100$ Hz. White lines depict boundaries of iso-i regions, and the black cross highlights the value of f_s^*/f_0 for the presented experimental cases **Ci**.

prescribed sinusoidal motion. For instance, Supplementary Fig. S1-c shows threshold values chosen (arbitrarily) so that the errors generated by motion artefacts do not exceed PCC ≈ 0.85 and SEVP $\approx 50\%$ (red areas): this would lead to fix the critical descriptors around $\beta_1^* \approx \beta_2^* \approx 5$ px in the case of spherical particles ($\beta_1^* \approx \beta_2^* \approx 2$ px in the case of fibrous particles; Supplementary Fig. S1-b). Knowing this, it is possible to determine a peak-to-peak oscillation amplitude A^* that should not be exceeded during the experiment (Fig. 1d).

Determination of the optimised sampling rate
Following the aforementioned guidelines, the optimised projection sampling rate, f_s^*, can also be determined for each specific configuration under study. Figure 6 displays all optimised values f_s^* predicted in the plane $(t_e + t_l, N)$ when $f_0 = 100$ Hz (Eq. 1) – note that equivalent graphs for $f_0 = 50$ Hz and $f_0 = 400$ Hz are given in Supplementary Fig. S2. It is shown that the same frequency f_s^* can be suitable for different triplets of parameters (t_e, t_l, N). More particularly, the case ($t_e \approx 0.8$ ms, $t_l \approx 0$ ms, $N = 30$), which was further selected for experiments **C1**, **C2** and **C3** (Table 1), yields to $f_s^* \approx 1{,}033$ Hz, as pointed out in Fig. 6 (see black cross). Note that such a configuration requires at least $i = 3$ oscillation periods to acquire $N = 30$ consecutive projections, and corresponds to case III in Fig. 2.

Experimental validation
General experimental trends
Figure 7 shows typical 2D slices of the composite reinforced with spherical glass beads, scanned under *reference static* conditions (panel a), tracked over $N = 30$ phases of its 100 Hz-vibration after gated-CT reconstruction (panel b), along with the quantitative analyses of the recorded 4D dataset (graphs c–e). An animation of the reconstructed slices over time is also available in Supplementary Video "C2_Sphere_100Hz_MR.gif". Results are here illustrated for case **C2** (Table 1), characterised by intermediate kinematics and motion blurs, i.e., with $A^* \approx 24$ px and $(\beta_1^*, \beta_2^*) \approx (6$ px, 2.5 px). Similar results are shown in Supplementary Figs. S3 and S4 for cases **C1** (amplitude A^* divided by half compared to **C2**) and **C3** (A^* increased by a factor of ≈ 1.5), respectively. Whatever the case, we were able to acquire, reconstruct and process the 30 phases of the sample's motion. Several general trends can be highlighted, as detailed below.

Angular sampling of projections—One of the main objectives of the optimisation procedure was to ensure a uniform angular distribution of projections for 3D dataset. The barplot of the actual number of projections per phase, reported in Fig. 7e, shows that this number varies little along the 30 phases, staying close to the initial target of $n \approx 330$. This first result evidences that a reasonable phase sampling was achieved. In addition, the polar histograms displayed in Fig. 7b provide an overview of the projection space. They confirm that the angular distribution of the projections for each phase remains almost uniform with minor clustering[74] as expected by the use of case III in Fig. 2. These results validate the proposed guideline.

Sample motion—The rigid translations in each direction estimated from the registration (see "Methods" section *Quality of the 3D images*) are plotted in Fig. 7c, relative to the phase number. Although a small shift of few micrometers can be noticed in the x and y axis direction due to the mechanical backlash of the system, most of the translation is measured along the z axis as a sine wave-like profile in agreement with the imposed excitation motion.

Image quality—The different CT-scans quality indices (PCC and SEVP) are presented in Fig. 7d for case **C2**, and in Supplementary Figs. S3-d and S4-d for cases (**C1**, **C3**). The detailed mean and extreme values of the indices are reported in Table 2 for each case.
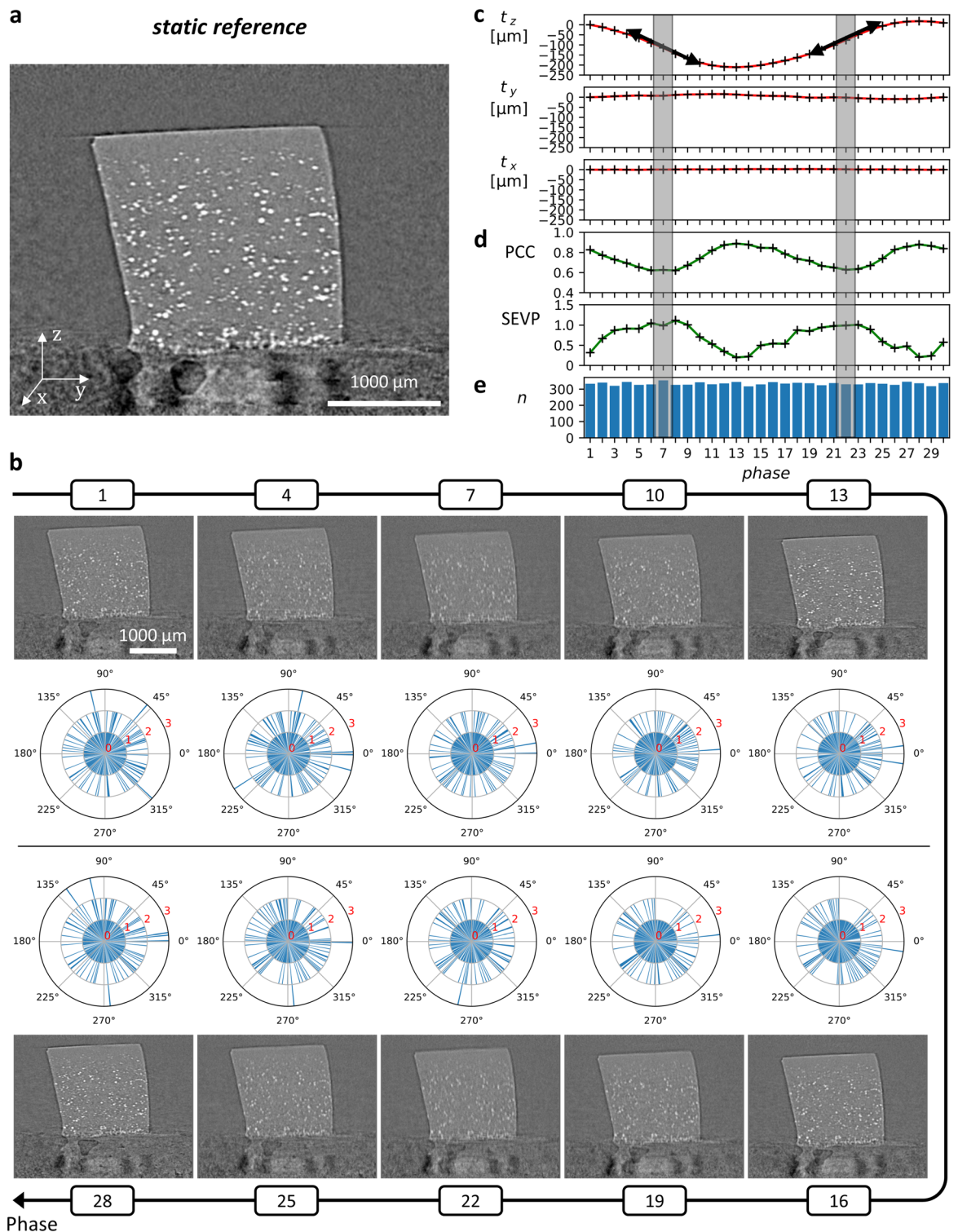
Figure 7. Example of typical optimised result for case study **C2**. (**a**) Vertical slice of the *static reference*. (**b**) 10 out of 30 vertical slices of the vibrating sample, and corresponding polar histograms of the angular sampling of projections (bin width = 1°). The supplementary Video "C2_Sphere_100Hz_MR.gif" provides a dynamic version of the vertical slices. (**c**) Plots of the measured 3D translation using rigid registration. Black arrows denote maximum slopes of the sinusoidal motion. **d.** Image quality metrics between the *static reference* and each of the 30 registered phases. Grey boxes depict phases with minimal image quality. (**e**) Barplot of the number of projections per phase n.
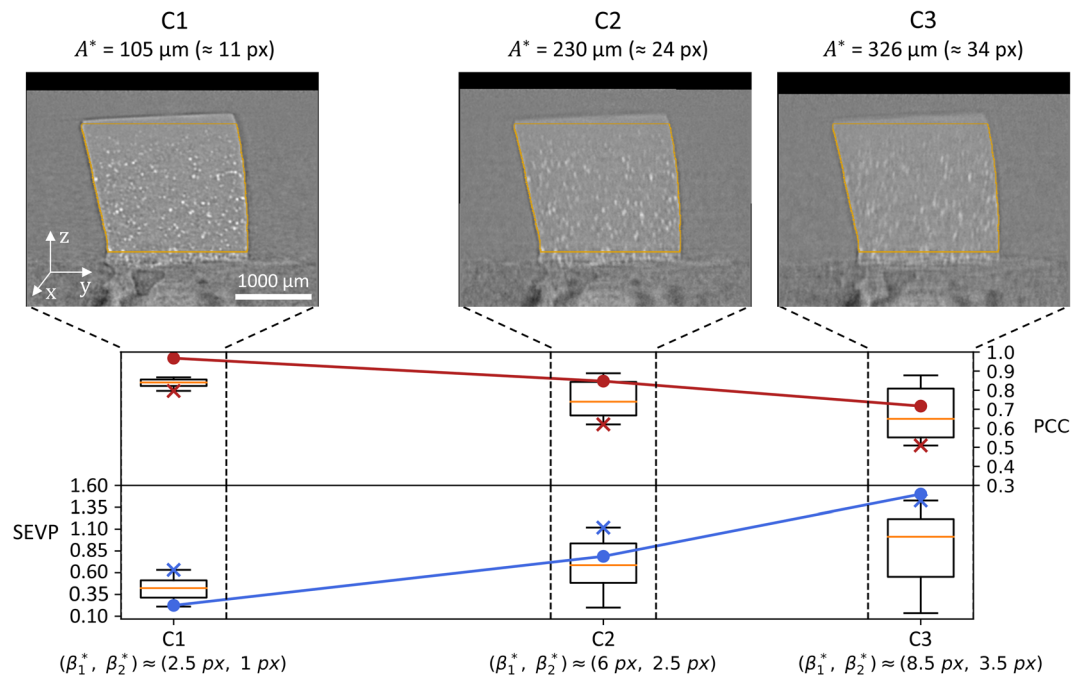
Figure 8. *(Top)* Vertical slices of registered volumes at maximum motion speed for each case studies. Orange outlines denote the boundaries of the ROI for PCC and SEVP computations. *(Bottom)* Boxplots of the result of image quality metrics between the *static reference* and each of the 30 registered phases for the three case studies, as a function of the blur descriptors. Crosses show the value for the specific phase that happened at the maximum speed, for which the blur descriptors are defined. The points denote the interpolated results of the tomography simulation for these specific couples β_1, β_2.

	C1				C2				C3			
	min	max	mean	std	min	max	mean	std	min	max	mean	std
PCC	0.80	0.87	0.84	0.02	0.62	0.89	0.75	0.09	0.51	0.88	0.67	0.13
SEVP	0.21	0.63	0.41	0.12	0.20	1.12	0.68	0.29	0.14	1.43	0.91	0.38

Table 2. Table of minimal, maximal, mean and standard deviation values of image quality metrics for each case studies.

Whether for PCC or SEVP, the poorest image quality is obtained when the translation speed approaches v_{max} (see shaded areas), thus when A^*, β_1^* and β_2^* are maximum, as shown by PCC (resp. SEVP) going from 0.84 to 0.67 (resp. 0.41 to 0.91) in average when A^* is tripled. Nakamura et al.[51] measured similar trends with a larger spherical phantom ($d_0^* = 16$), correlating volumetric error to the phantom maximum velocity.

For all case studies, Fig. 8 summarises the evolution of the two quality indices measured over the 30 phases of the sinusoidal translation, by means of box plots highlighting the statistical values detailed in Table 2. The degradation of the metrics along with the increase of blur descriptors is clearly observed, which are, by definition, relative to the phase with maximum motion speed (see crosses). Besides, the maximum values of PCC (respectively the minimum ones of SEVP), which correspond to oscillation phase with minimal motion speed, stay almost constant along the three case studies (i.e., max PCC ≈ 0.88). This observation suggests that the motion blur is presumably the main cause of image quality degradation. However, other sources could also enhance this gap: the registration uncertainties, the angular distribution of the projections which is not as perfect as for the *static reference* (Fig. 7b), and the inherent random electronic noise.

Comparison between experimental data and numerical predictions
Figure 8 also presents the comparison between experimental results and numerical predictions of the image quality indices PCC and SEVP, as derived from particle-scale simulations (Fig. 5). In both approaches, the size of spherical heterogeneities were deliberately kept in the same range ($d_0^* \approx 4$) to allow suitable comparison.

Experimental and numerical data follow interestingly the same qualitative trends over the 30 phases. From a quantitative point of view, despite a reasonable agreement overall, the simulations overestimate image quality for almost all the screened couples (β_1^*, β_2^*). The uncertainty factors mentioned in the previous section could explain such a discrepancy, notably the measurement noise linked to the acquisition and which has not been simulated.

In addition, with regards to SEVP, image degradation increases more rapidly with blur according to numerical predictions than experimentally. The fact that the contrast ratio between particles and background is about three times higher in the phantom than in real gated-CT's ROI may partly explain these differences. Choosing a lower contrast between particles and image background in the phantom would have led to a rapid combination of grey levels with the blur. In this case, the histogram-based segmentation would have been more ambiguous, and the derived volume of heterogeneities less overestimated.

In summary, despite all assumptions, for bead-reinforced composites with moderate vibrating amplitudes (up to $\approx$ 250 μm) and frequencies (up to 100 Hz), the proposed modeling gives relevant guidelines to predict how much the motion blur affects the final image quality of most critical phases, and to select suitable acquisition parameters.

Performances of the optimisation guidelines

The performances of the optimisation guidelines detailed above and validated for a limited set of kinematical, geometrical and X-ray scanning parameters (cases **Ci**, $i = \{1, 2, 3\}$) were further assessed for wider configurations. In particular, a selection of three other cases pushing each set of parameters towards extreme values is illustrated in Supplementary Fig. S5 (see Supplementary Methods for technical details), showing the versatility of the measurement strategy and optimisation procedure:

- the case of a higher oscillation frequency ($f_0 = 400$ Hz), which required optimal values $A^* \approx 9$ px (≈ 86 μm with unchanged pixel size), $\beta_1^* \approx 2$ px, $\beta_2^* \approx 1$ px, $f_s^* \approx 4{,}133$ Hz (see Supplementary Video "Sphere_400Hz_MR.gif");
- the case of other heterogeneous media owning a structural anisotropy (fibrous particles), which required optimal values $A^* \approx 30$ px (≈ 287 μm with unchanged pixel size), $\beta_1^* \approx 7.5$ px, $\beta_2^* \approx 3$ px, $f_s^* \approx 1{,}033$ Hz (see Supplementary Video "Fibre_100Hz_MR.gif");
- the case of higher magnification ($L_{vx} = 2.17$ μm) with optimal values $A^* \approx 105$ px (≈ 228 μm), $\beta_1^* \approx 5$ px, $\beta_2^* \approx 11$ px, $f_s^* \approx 3{,}000$ Hz (see Supplementary Video "Sphere_100Hz_HR.gif").

The methodology was successfully applied to all cases, enabling the efficient reconstruction of 4D images of fast vibrating structures with controlled and limited blur artefacts, i.e., an essential step for future multi-scale quantitative analyses[57]. However, several limitations were observed for most extreme cases. To achieve the case at $f_0 = 400$ Hz, the exposure time was first reduced by a factor of 4 ($t_e \approx 0.2$ ms) so as to maintain a blur motion β_1^*-level (and therefore, a vibratory amplitude A^*) nearly constant compared to previous cases **Ci** at $f_0 = 100$ Hz (see Supplementary Fig. S2 in case $f_0 = 400$ Hz). However, given the lower vibration amplitudes allowed by the electromechanical shaker at $f_0 = 400$ Hz, we were forced to reduce A^* even further in this case (by a few pixels), thus reaching the upper limit possible. Besides, this configuration brought us close to the capacity limits of the detector used in this study. In practice, if the method were to be extended to even higher oscillation frequencies, the use of a detector allowing shorter exposure times would be recommended[44,76]. At highest magnification, the X-ray flux was increased almost by an order of magnitude, inducing obvious material damage after a few scans on the same composite. For such cases, the use of dose-attenuation equipment, such as synchronised rotating X-ray shutter[42,48], could be evaluated if the methodology leads to relatively long latency time t_l^* between projections. Future optical and detector systems that can better convert photons into signal will also be helpful in reducing the dose. Overall, these results obtained with relatively simple microstructured soft composites are transferable to materials with a more complex structure such as biological tissues.

Finally, Fig. 9 displays a range of reference studies conducted to image structures and systems likely to evolve periodically over time using microtomography, accounting for various X-ray sources (medical, laboratory or synchrotron) and scanning strategies (prospective gating, retrospective gating or no gating). Each study can be characterised by its spatiotemporal resolution, based on the prescribed pixel size of the acquisition, and the achieved temporal resolution (or equivalent scan rate). It is important to keep in mind that this map does not display the velocity of the captured motion, nor the sensitivity of the sample to the radiation dose, the degree of quantitativeness of the resulting 4D images or the achieved FOV. However, it gives meaningful insights for the current limits of gated-CT for periodic or quasi-periodic motions. In particular, the areas that are currently accessible using conventional equipment and/or conventional time-resolved X-ray tomography are highlighted. Hence, Fig. 9 shows that the present measurement strategy has made it possible to image a multiscale oscillator in a simple rigid body motion, but reaching the spatiotemporal limits currently acquired by gated-CT, with equivalent scan rates from 3000 up to 12,000 tomographies per second. Our approach now offers a validated method for optimising the acquisition of 4D images of fast-oscillating structures scanned in this high-performance region in terms of spatiotemporal resolution (see red region in Fig. 9), and for predicting their quality using quantitative metrics. By providing a solid basis for imaging heterogeneous 3D structures oscillating at high frequency during simple, controlled translation, this work paves the way for a wide range of research aimed at characterising the 3D deformations of more complex vibrators.

Conclusion

The general objective of this work was to improve the acquisition and reconstruction procedures of retrospectively gated X-ray CT in order to image and study the 3D motion of structures oscillating at high frequencies. More specifically, our approach aimed to minimise streaking and blurring artefacts typically obtained when imaging a moving structure. To this end, numerical guidelines are provided for optimising the acquisition parameters, by predicting on the one hand the conditions for quasi-regular angular sampling of projections with minor clustering, and on the other hand the level of image quality degradation as a function of two main types
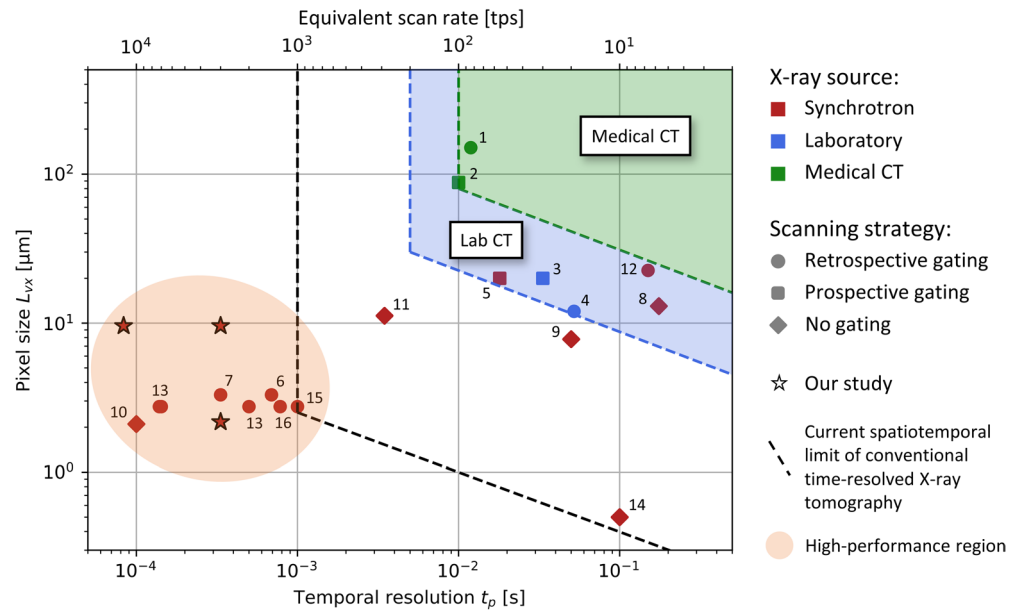
Figure 9. Spatiotemporal resolution expressed as pixel size *versus* phase width for state of the art CT applied to the imaging of periodic systems. The current limit for conventional time-resolved X-ray tomography was proposed by García-Moreno et al.[19]. Boundaries for laboratory and clinical-CT were approximated from the latter trend. The database on which this figure is based is available in Supplementary Table S1. (1) Drangova et al.[28], (2) Guo et al.[32], (3) Murrie et al.[33], (4) Schuler et al.[40], (5) Dubsky et al.[46], (6) Walker et al.[38], (7) Mokso et al.[21], (8) Hoshino et al.[47], (9) Hoshino et al.[75], (10) Tekawade et al.[49], (11) Wu et al.[42], (12) Fardin et al.[29], (13) Maiditsch et al.[4], (14) Matsubara et al.[48], (15) Dejea et al.[3], (16) Schmeltz et al.[5].

of motion blur. It is shown that these conditions highly depend on the triplet formed by the vibrating-structure mean frequency, the beam exposure time per projection, and the number of temporal phases to be reconstructed in order to obtain a discrete sequence of oscillation cycle. The guidelines were validated experimentally by a series of synchrotron experiments, which made it possible to image rigid-body motions of elastomers reinforced with microparticles while vibrating at 100 Hz up to 400 Hz, achieving an equivalent rate of 3000 up to 12,000 tomographies per second with controlled and limited blurring artefacts.

This work opens the way to a number of methodological perspectives and research applications. Image quality can be improved by coupling the technique to reconstruction algorithms using deep learning assisted methods[77–79]. The proposed methodology can be extended to lab microtomography with cone beam X-ray sources, although the achievable spatiotemporal resolution decreases by several orders of magnitude in this case (due to a typical projection sampling rate of the order of a few tens of Hz at most, depending on the configuration)[33,40]. These developments can be combined with kinematic field measurements to further characterize the 3D deformation of microstructured oscillators[48,57].

Data availability
The datasets generated and/or analysed during the current study are available from the corresponding author upon request.

References
1. Ford, N. L. *et al.* Prospective respiratory-gated micro-CT of free breathing rodents. *Med. Phys.* **32**, 2888–2898. https://doi.org/10.1118/1.2013007 (2005).
2. Lovric, G. *et al.* Tomographic in vivo microscopy for the study of lung physiology at the alveolar level. *Sci. Rep.* **7**, 12545. https://doi.org/10.1038/s41598-017-12886-3 (2017).
3. Dejea, H. *et al.* A tomographic microscopy-compatible Langendorff system for the dynamic structural characterization of the cardiac cycle. *Front. Cardiovasc. Med.* **9**, 1023483. https://doi.org/10.3389/fcvm.2022.1023483 (2022).
4. Maiditsch, I. P., Ladich, F., Heß, M., Schlepütz, C. M. & Schulz-Mirbach, T. Revealing sound-induced motion patterns in fish hearing structures in 4D: A standing wave tube-like setup designed for high-resolution time-resolved tomography. *J. Exp. Biol.* **225**, jeb243614. https://doi.org/10.1242/jeb.243614 (2022).
5. Schmeltz, M. *et al.* The human middle ear in motion: 3D visualization and quantification using dynamic synchrotron-based X-ray imaging. *Commun. Biol.* **7**, 157. https://doi.org/10.1038/s42003-023-05738-6 (2024).
6. Titze, I. R. *Principles of voice production* 2nd edn. (National Center for Voice and Speech, 2000).
7. Luizard, P. *et al.* Flow-induced oscillations of vocal-fold replicas with tuned extensibility and material properties. *Sci. Rep.* **13**, 22658. https://doi.org/10.1038/s41598-023-48080-x (2023).

8. Timcke, R. Die Synchron-Stroboskopie von menschlichen Stimmlippen bzw. ähnlichen Schallquellen und Messung der Öffnungs-zeit [Synchronous stroboscopy of the vocal cords in man and analogous sources of sound and the duration of opening]. *Laryngol. Rhinol. Otol.* **35**, 331–5 (1956).

9. Švec, J. G. & Schutte, H. K. Videokymography: High-speed line scanning of vocal fold vibration. *J. Voice* **10**, 201–205. https://doi.org/10.1016/S0892-1997(96)80047-6 (1996).

10. Schutte, H. K., Svec, J. G. & Sram, F. First results of clinical application of videokymography. *Laryngoscope* **108**, 1206–10. https://doi.org/10.1097/00005537-199808000-00020 (1998).

11. Deliyski, D. D. & Hillman, R. E. State of the art laryngeal imaging: Research and clinical implications. *Curr. Opin. Otolaryngol. Head Neck Surg.* **18**, 147–152. https://doi.org/10.1097/MOO.0b013e3283395dd4 (2010).

12. Baken, R. & Orlikoff, R. F. *Clinical measurement of speech and voice* (Singular, 2000).

13. Ziethe, A., Patel, R., Kunduk, M., Eysholdt, U. & Graf, S. Clinical analysis methods of voice disorders. *Curr. Bioinform.* **6**, 270–285. https://doi.org/10.2174/157489311796904682 (2011).

14. Andrade-Miranda, G., Stylianou, Y., Deliyski, D. D., Godino-Llorente, J. I. & Henrich Bernardoni, N. Laryngeal image processing of vocal folds motion. *Appl. Sci.* **10**, 1556. https://doi.org/10.3390/app10051556 (2020).

15. Bailly, L. *et al.* 3D multiscale imaging of human vocal folds using synchrotron X-ray microtomography in phase retrieval mode. *Sci. Rep.* **8**, 14003. https://doi.org/10.1038/s41598-018-31849-w (2018).

16. Olbinado, M. P., Vagovič, P., Yashiro, W. & Momose, A. Demonstration of stroboscopic X-ray talbot interferometry using polychromatic synchrotron and laboratory X-ray sources. *Appl. Phys. Express* **6**, 096601. https://doi.org/10.7567/APEX.6.096601 (2013).

17. Schulz-Mirbach, T. *et al.* In-situ visualization of sound-induced otolith motion using hard X-ray phase contrast imaging. *Sci. Rep.* **8**, 3121. https://doi.org/10.1038/s41598-018-21367-0 (2018).

18. Schulz-Mirbach, T. *et al.* Auditory chain reaction: Effects of sound pressure and particle motion on auditory structures in fishes. *PLoS ONE* **15**, e0230578. https://doi.org/10.1371/journal.pone.0230578 (2020).

19. García-Moreno, F. *et al.* Tomoscopy: Time-resolved tomography for dynamic processes in materials. *Adv. Mater.* **33**, 2104659. https://doi.org/10.1002/adma.202104659 (2021).

20. dos Santos Rolo, T., Ershov, A., van de Kamp, T. & Baumbach, T. In vivo X-ray cine-tomography for tracking morphological dynamics. *Proc. Natl. Acad. Sci.* **111**, 3921–3926. https://doi.org/10.1073/pnas.1308650111 (2014).

21. Mokso, R. *et al.* Four-dimensional in vivo X-ray microscopy with projection-guided gating. *Sci. Rep.* **5**, 8727. https://doi.org/10.1038/srep08727 (2015).

22. Maire, E., Le Bourlot, C., Adrien, J., Mortensen, A. & Mokso, R. 20 Hz X-ray tomography during an in situ tensile test. *Int. J. Fract.* **200**, 3–12. https://doi.org/10.1007/s10704-016-0077-y (2016).

23. Laurencin, T. *et al.* 3D real-time and in situ characterisation of fibre kinematics in dilute non-Newtonian fibre suspensions during confined and lubricated compression flow. *Compos. Sci. Technol.* **134**, 258–266. https://doi.org/10.1016/j.compscitech.2016.09.004 (2016).

24. Ferré Sentis, D. *et al.* 3D in situ observations of the compressibility and pore transport in Sheet Moulding Compounds during the early stages of compression moulding. *Compos. A Appl. Sci. Manuf.* **92**, 51–61. https://doi.org/10.1016/j.compositesa.2016.10.031 (2017).

25. Laurencin, T. *et al.* 3D real time and in situ observation of the fibre orientation during the plane strain flow of concentrated fibre suspensions. *J. Nonnewton. Fluid Mech.* **312**, 104978. https://doi.org/10.1016/j.jnnfm.2022.104978 (2023).

26. Amedewovo, L. *et al.* Deconsolidation of carbon fiber-reinforced PEKK laminates: 3D real-time in situ observation with synchrotron X-ray microtomography. *Compos. A Appl. Sci. Manuf.* **177**, 107917. https://doi.org/10.1016/j.compositesa.2023.107917 (2024).

27. Keall, P. J., Kini, V. R., Vedam, S. S. & Mohan, R. Potential radiotherapy improvements with respiratory gating. *Australas. Phys. Eng. Sci. Med.* **25**, 1–6. https://doi.org/10.1007/BF03178368 (2002).

28. Drangova, M., Ford, N. L., Detombe, S. A., Wheatley, A. R. & Holdsworth, D. W. Fast retrospectively gated quantitative four-dimensional (4D) cardiac micro computed tomography imaging of free-breathing mice. *Invest. Radiol.* **42**, 85–94. https://doi.org/10.1097/01.rli.0000251572.56139.a3 (2007).

29. Fardin, L. *et al.* Imaging atelectrauma in ventilator-induced lung injury using 4D X-ray microscopy. *Sci. Rep.* **11**, 4236. https://doi.org/10.1038/s41598-020-77300-x (2021).

30. Badea, C., Hedlund, L. W. & Johnson, G. A. Micro-CT with respiratory and cardiac gating: Micro-CT with respiratory and cardiac gating. *Med. Phys.* **31**, 3324–3329. https://doi.org/10.1118/1.1812604 (2004).

31. Badea, C. T., Fubara, B., Hedlund, L. W. & Johnson, G. A. 4-D micro-CT of the mouse heart. *Mol. Imaging* **4**, 153535002005041. https://doi.org/10.1162/15353500200504187 (2005).

32. Guo, X., Johnston, S. M., Qi, Y., Johnson, G. A. & Badea, C. T. 4D micro-CT using fast prospective gating. *Phys. Med. Biol.* **57**, 257–271. https://doi.org/10.1088/0031-9155/57/1/257 (2012).

33. Murrie, R. P. *et al.* Real-time in vivo imaging of regional lung function in a mouse model of cystic fibrosis on a laboratory X-ray source. *Sci. Rep.* **10**, 447. https://doi.org/10.1038/s41598-019-57376-w (2020).

34. Manzke, R., Köhler, Th., Nielsen, T., Hawkes, D. & Grass, M. Automatic phase determination for retrospectively gated cardiac CT: Automatic phase determination for retrospectively gated cardiac CT. *Med. Phys.* **31**, 3345–3362. https://doi.org/10.1118/1.1791351 (2004).

35. Hu, J., Haworth, S. T., Molthen, R. C. & Dawson, C. A. Dynamic small animal lung imaging via a postacquisition respiratory gating technique using micro-cone beam computed tomography1. *Acad. Radiol.* **11**, 961–970. https://doi.org/10.1016/j.acra.2004.05.019 (2004).

36. Sonke, J.-J., Zijp, L., Remeijer, P. & van Herk, M. Respiratory correlated cone beam CT: Respiratory correlated cone beam CT. *Med. Phys.* **32**, 1176–1186. https://doi.org/10.1118/1.1869074 (2005).

37. Ford, N. L., Wheatley, A. R., Holdsworth, D. W. & Drangova, M. Optimization of a retrospective technique for respiratory-gated high speed micro-CT of free-breathing rodents. *Phys. Med. Biol.* **52**, 5749–5769. https://doi.org/10.1088/0031-9155/52/19/002 (2007).

38. Walker, S. M. *et al.* In vivo time-resolved microtomography reveals the mechanics of the blowfly flight motor. *PLoS Biol.* **12**, e1001823. https://doi.org/10.1371/journal.pbio.1001823 (2014).

39. Fardin, L. *In-vivo dynamic 3D phase-contrast microscopy: A novel tool to investigate the mechanisms of ventilator induced lung injury*. Ph.D. thesis, Université Grenoble Alpes (2019).

40. Schuler, J., Neuendorf, L. M., Petersen, K. & Kockmann, N. Micro-computed tomography for the 3D time-resolved investigation of monodisperse droplet generation in a co-flow setup. *AIChE J.* https://doi.org/10.1002/aic.17111 *(2021)*.

41. Paganin, D., Mayo, S. C., Gureyev, T. E., Miller, P. R. & Wilkins, S. W. Simultaneous phase and amplitude extraction from a single defocused image of a homogeneous object. *J. Microsc.* **206**, 33–40. https://doi.org/10.1046/j.1365-2818.2002.01010.x (2002).

42. Wu, Y., Takano, H. & Momose, A. Time-resolved x-ray stroboscopic phase tomography using Talbot interferometer for dynamic deformation measurements. *Rev. Sci. Instrum.* **92**, 043702. https://doi.org/10.1063/5.0030811 (2021).

43. Lovric, G., Mokso, R., Schlepütz, C. M. & Stampanoni, M. A multi-purpose imaging endstation for high-resolution micrometer-scaled sub-second tomography. *Physica Med.* **32**, 1771–1778. https://doi.org/10.1016/j.ejmp.2016.08.012 (2016).

44. Mokso, R. *et al.* GigaFRoST: The gigabit fast readout system for tomography. *J. Synchrotron Radiat.* **24**, 1250–1259. https://doi.org/10.1107/S1600577517013522 (2017).

45. Maire, E. & Withers, P. J. Quantitative X-ray tomography. *Int. Mater. Rev.* **59**, 1–43. https://doi.org/10.1179/1743280413Y.0000000023 (2014).
46. Dubsky, S., Hooper, S. B., Siu, K. K. W. & Fouras, A. Synchrotron-based dynamic computed tomography of tissue motion for regional lung function measurement. *J. R. Soc. Interface* **9**, 2213–2224. https://doi.org/10.1098/rsif.2012.0116 (2012).
47. Hoshino, M., Uesugi, K. & Yagi, N. 4D x-ray phase contrast tomography for repeatable motion of biological samples. *Rev. Sci. Instrum.* **87**, 093705. https://doi.org/10.1063/1.4962405 (2016).
48. Matsubara, M. *et al.* Dynamic observation of a damping material using micro X-ray computed tomography coupled with a phase-locked loop. *Polym. Test.*https://doi.org/10.1016/j.polymertesting.2022.107810 *(2022).*
49. Tekawade, A. *et al.* Time-resolved 3D imaging of two-phase fluid flow inside a steel fuel injector using synchrotron X-ray tomography. *Sci. Rep.* **10**, 8674. https://doi.org/10.1038/s41598-020-65701-x (2020).
50. Herrmann, J., Hoffman, E. A. & Kaczka, D. W. Frequency-selective computed tomography: Applications during periodic thoracic motion. *IEEE Trans. Med. Imaging* **36**, 1722–1732. https://doi.org/10.1109/TMI.2017.2694887 (2017).
51. Nakamura, M. *et al.* Impact of motion velocity on four-dimensional target volumes: A phantom study: Impact of motion velocity on 4D target volumes. *Med. Phys.* **36**, 1610–1617. https://doi.org/10.1118/1.3110073 (2009).
52. Li, T. *et al.* Four-dimensional cone-beam computed tomography using an on-board imager. *Med. Phys.* **33**, 3825–3833. https://doi.org/10.1118/1.2349692 (2006).
53. Yamamoto, T., Langner, U., Loo, B. W., Shen, J. & Keall, P. J. Retrospective analysis of artifacts in four-dimensional CT images of 50 abdominal and thoracic radiotherapy patients. *Int. J. Radiat. Oncol. Biol. Phys.* **72**, 1250–1258. https://doi.org/10.1016/j.ijrobp.2008.06.1937 (2008).
54. Rueckel, J., Stockmar, M., Pfeiffer, F. & Herzen, J. Spatial resolution characterization of a X-ray microCT system. *Appl. Radiat. Isot.* **94**, 230–234. https://doi.org/10.1016/j.apradiso.2014.08.014 (2014).
55. McCullough, E. C. *et al.* Performance evaluation and quality assurance of computed tomography scanners, with illustrations from the EMI, ACTA, and delta scanners. *Radiology* **120**, 173–188. https://doi.org/10.1148/120.1.173 (1976).
56. García-Moreno, F. *et al.* Using X-ray tomoscopy to explore the dynamics of foaming metal. *Nat. Commun.* **10**, 3762. https://doi.org/10.1038/s41467-019-11521-1 (2019).
57. Stamati, O. *et al.* Spam: Software for practical analysis of materials. *J. Open Source Softw.* **5**, 2286. https://doi.org/10.21105/joss.02286 (2020).
58. Stamati, O. *et al.* Advanced analysis of the bias-extension of woven fabrics with X-ray microtomography and Digital Volume Correlation. *Compos. A Appl. Sci. Manuf.* **175**, 107748. https://doi.org/10.1016/j.compositesa.2023.107748 (2023).
59. Barrett, J. F. & Keat, N. Artifacts in CT: Recognition and avoidance. *Radiographics* **24**, 1679–1691. https://doi.org/10.1148/rg.246045065 (2004).
60. Depriester, D. *et al.* Individual fibre separation in 3D fibrous materials imaged by X-ray tomography. *J. Microsc.* **286**, 220–239. https://doi.org/10.1111/jmi.13096 (2022).
61. O'Brien, R. T., Cooper, B. J. & Keall, P. J. Optimizing 4D cone beam computed tomography acquisition by varying the gantry velocity and projection time interval. *Phys. Med. Biol.* **58**, 1705–1723. https://doi.org/10.1088/0031-9155/58/6/1705 (2013).
62. Park, J. C. *et al.* Four dimensional digital tomosynthesis using on-board imager for the verification of respiratory motion. *PLoS ONE* **9**, e115795. https://doi.org/10.1371/journal.pone.0115795 (2014).
63. Withers, P. J. *et al.* X-ray computed tomography. *Nat. Rev. Methods Primers* **1**, 18. https://doi.org/10.1038/s43586-021-00015-4 (2021).
64. Tengattini, A. & Andò, E. Kalisphera: An analytical tool to reproduce the partial volume effect of spheres imaged in 3D. *Meas. Sci. Technol.* **26**, 095606. https://doi.org/10.1088/0957-0233/26/9/095606 (2015).
65. Palenstijn, W., Batenburg, K. & Sijbers, J. Performance improvements for iterative electron tomography reconstruction using graphics processing units (GPUs). *J. Struct. Biol.* **176**, 250–253. https://doi.org/10.1016/j.jsb.2011.07.017 (2011).
66. van Aarle, W. *et al.* The ASTRA Toolbox: A platform for advanced algorithm development in electron tomography. *Ultramicroscopy* **157**, 35–47. https://doi.org/10.1016/j.ultramic.2015.05.002 (2015).
67. van Aarle, W. *et al.* Fast and flexible X-ray tomography using the ASTRA toolbox. *Opt. Express* **24**, 25129. https://doi.org/10.1364/OE.24.025129 (2016).
68. King, A. *et al.* Tomography and imaging at the PSICHE beam line of the SOLEIL synchrotron. *Rev. Sci. Instrum.* **87**, 093704. https://doi.org/10.1063/1.4961365 (2016).
69. King, A. *et al.* Recent tomographic imaging developments at the PSICHE beamline. *Integrating Mater. Manuf. Innov.* **8**, 551–558. https://doi.org/10.1007/s40192-019-00155-2 (2019).
70. Mirone, A., Brun, E., Gouillart, E., Tafforeau, P. & Kieffer, J. The PyHST2 hybrid distributed code for high speed tomographic reconstruction with iterative reconstruction and a priori knowledge capabilities. *Nucl. Instrum. Methods Phys. Res. Sect. B* **324**, 41–48. https://doi.org/10.1016/j.nimb.2013.09.030 (2014).
71. Rodgers, J. L. & Nicewander, W. A. Thirteen ways to look at the correlation coefficient. *Am. Stat.* **42**, 59. https://doi.org/10.2307/2685263 (1988) arXiv:2685263.
72. Otsu, N. A threshold selection method from gray-level histograms. *IEEE Trans. Syst. Man Cybern.* **9**, 62–66. https://doi.org/10.1109/TSMC.1979.4310076 (1979).
73. Rietzel, E., Pan, T. & Chen, G. T. Y. Four-dimensional computed tomography: Image formation and clinical protocol: 4D computed tomography. *Med. Phys.* **32**, 874–889. https://doi.org/10.1118/1.1869852 (2005).
74. Cooper, B. J., O'Brien, R. T., Balik, S., Hugo, G. D. & Keall, P. J. Respiratory triggered 4D cone-beam computed tomography: A novel method to reduce imaging dose: RT 4DCBCT: A novel method reducing imaging dose. *Med. Phys.* **40**, 041901. https://doi.org/10.1118/1.4793724 (2013).
75. Hoshino, M., Uesugi, K., Yagi, N. & Tsukube, T. Improvement of scanning procedure for 4D-X-ray phase tomography. *Microscopy and Microanalysis*. **24**(S2), 130–131. https://doi.org/10.1017/S1431927618013041 (2018).
76. Pfaff, J. *et al.* In Situ chamber for studying battery failure using high-speed synchrotron radiography. *J. Synchrotron Radiat.* **30**, 192–199. https://doi.org/10.1107/S1600577522010244 (2023).
77. Pelt, D., Batenburg, K. & Sethian, J. Improving tomographic reconstruction from limited data using mixed-scale dense convolutional neural networks. *J. Imaging* **4**, 128. https://doi.org/10.3390/jimaging4110128 (2018).
78. Hendriksen, A. A., Pelt, D. M. & Batenburg, K. J. Noise2Inverse: Self-supervised deep convolutional denoising for tomography. *IEEE Trans. Comput. Imaging* **6**, 1320–1335. https://doi.org/10.1109/TCI.2020.3019647 (2020).
79. Liu, Z. *et al.* TomoGAN: Low-dose synchrotron x-ray tomography with generative adversarial networks: Discussion. *J. Opt. Soc. Am. A* **37**, 422. https://doi.org/10.1364/JOSAA.375595 (2020).

Acknowledgements

Author contributions

L.Ba., S.R.R., L.O. and N.H.B. conceptualised the research, and co-supervised the study. A.Kl. developed the theoretical framework, designed and built the experimental setup. He conducted the experiments, conceived and performed simulations, and was the main investigator for post-processing and data analysis. L.Br. and A.Ki. provided technical expertise in beamline instrumentation and data post-processing. A.Ki. configured the imaging setup and operated the synchrotron beamline. L.Br. and A.Kl. coded the post-processing of the data to make the tomographic reconstruction available on the beamline during the experiments. All authors participated in the collection of experimental data. L.Ba., S.R.R., L.O. and N.H.B. contributed to the theoretical framework, to the data analysis, and to the interpretation of results. L.Ba. directed the project and was the main investigator for funding acquisition. A.Kl. drafted the manuscript and designed the figures. All authors contributed to manuscript revision, read, and approved the submitted version.

Competing interests

The authors declare no competing interests.

Additional information

Supplementary Information The online version contains supplementary material available at https://doi.org/10.1038/s41598-024-68684-1.

Correspondence and requests for materials should be addressed to L.B.

Reprints and permissions information is available at www.nature.com/reprints.

Publisher's note Springer Nature remains neutral with regard to jurisdictional claims in published maps and institutional affiliations.